

Resolution-Optimal Motion Planning for Steerable Needles

Mengyu Fu¹, Kiril Solovey², Oren Salzman², and Ron Alterovitz¹

Abstract—Medical steerable needles can follow 3D curvilinear trajectories inside body tissue, enabling them to move around critical anatomical structures and precisely reach clinically significant targets in a minimally invasive way. Automating needle steering, with motion planning as a key component, has the potential to maximize the accuracy, precision, speed, and safety of steerable needle procedures. In this paper, we introduce the first resolution-optimal motion planner for steerable needles that offers excellent practical performance in terms of runtime while simultaneously providing strong theoretical guarantees on completeness and the global optimality of the motion plan in finite time. Compared to state-of-the-art steerable needle motion planners, simulation experiments on realistic scenarios of lung biopsy demonstrate that our proposed planner is faster in generating higher-quality plans while incorporating clinically relevant cost functions. This indicates that the theoretical guarantees of the proposed planner have a practical impact on the motion plan quality, which is valuable for computing motion plans that minimize patient trauma.

I. INTRODUCTION

Medical steerable needles have the potential to improve patient care in diagnostic and therapeutic procedures including biopsy, localized drug delivery, and radioactive seed implantation for cancer treatment [4]. Steerable needles have a small diameter and are made of a highly flexible material, which allows them to follow 3D curvilinear trajectories inside the tissue. These properties enable steerable needles to move around critical anatomical structures to reduce patient trauma and reach sites previously unreachable with traditional straight needles [5–8].

Automating needle steering can improve the accuracy, precision, speed, and safety of steerable-needle procedures. Automating these procedures can also facilitate their broad use, since manual control of a steerable needle is challenging due to the nonholonomic constraints on the needle’s motion and the high level of precision required to operate it. A key component of automating steerable needle procedures is motion planning: computing feasible, obstacle-avoiding trajectories through the tissue to reach a target. The trajectory of the needle through tissue should also maximize

This project was supported in part by the United States National Institutes of Health (NIH) under award R01EB024864; the United States National Science Foundation (NSF) under awards 2008475 and 2038855; the Israeli Ministry of Science, Technology and Space (MOST) under awards 3-17385 and 3-16079; and the United States-Israel Binational Science Foundation (BSF) under award 2019703.

Code is available at [1].

¹M. Fu and R. Alterovitz are with the Department of Computer Science, University of North Carolina at Chapel Hill, Chapel Hill, NC 27599, USA. {mfu, ron}@cs.unc.edu

²K. Solovey and O. Salzman are with Computer Science Department, Technion - Israel Institute of Technology, Israel. kirilisol@stanford.edu, osalzman@cs.technion.ac.il

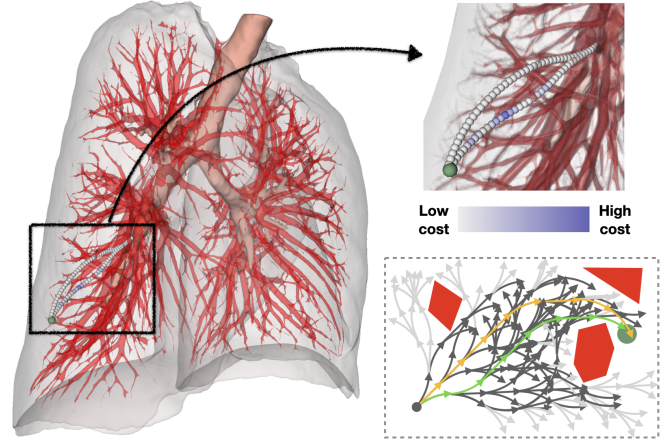


Fig. 1: **Left:** Overview of two different steerable-needle motion plans, both reaching a nodule (green) in the lung parenchyma for biopsy or cancer treatment while avoiding critical anatomical structures such as the bronchial tubes (brown) and major blood vessels (red). **Top right:** A zoomed-in view of two different plans where small blood vessels are rendered in grayscale. We use the method in [2] to reconstruct a cost map that represents the risk of puncturing small blood vessels. Different colors along the plans show different costs on the cost map. The top plan is computed with our proposed planner, RCS*. The bottom plan is computed with our previous RCS algorithm [3] and has a higher cost. **Bottom right:** A 2D illustration of the tree grown using our resolution-optimal motion planner towards a goal region (green) while avoiding obstacles (red). The best (shortest) plan found is shown in light green, and another valid but worse (longer) plan is shown in yellow. With a combination of generic and domain-specific optimizations, we can greatly shrink the search space (i.e., discard the light gray edges).

patient safety, which can be quantified using metrics such as minimizing trajectory length [9], maximizing clearance from obstacles [10–13], and minimizing damage to sensitive tissue [2, 14]. An example is shown in Fig. 1.

A motion planner for steerable needles should ideally offer guarantees on both finite-time completeness (i.e., compute in finite time a motion plan or indicate that none exists) and optimality (i.e., return a globally optimal motion plan with respect to a chosen cost metric). Most prior motion planners for steerable needles lack one or both of these criteria. For instance, some methods for steerable needle motion planning lack completeness guarantees [9, 15–20], and so may fail to find a motion plan when one exists. Some methods do aim to optimize motion plan cost but they lack *global* optimality guarantees [9, 20, 21].

Some sampling-based planners are known to be both complete and optimal, albeit those properties are usually proven only for an asymptotic regime where the number of samples tends to infinity [22–30]. Thus, it is unclear what should be the number of samples necessary to achieve those

guarantees in practice. Recent work has developed optimality guarantees for finite sampling, although those results cannot be currently applied to steerable needles as they deal with holonomic systems [31, 32].

In this paper, we introduce the first motion planner for steerable needles that offers excellent practical performance in terms of runtime while providing strong theoretical guarantees on completeness and the cost of the motion plan in *finite time*. In particular, we consider a specific type of optimality in relation to the motion plan cost—resolution optimality. Generally speaking, a resolution characterizes the discretization of some space (e.g., state space, configuration space, action space, and time). An algorithm is *resolution complete* if there exists a fine-enough resolution with which the algorithm finds a motion plan in finite time when a qualified motion plan exists, and otherwise correctly returns that no such plan exists [3]. An algorithm is *resolution optimal* if it is resolution complete and if, when it does return a motion plan, the plan’s cost is guaranteed to be within a desired approximation factor of the cost of a globally optimal qualified motion plan.

Our new motion planner builds on Resolution-Complete Search (RCS) [3], which is a resolution-complete but not resolution-optimal motion planner for steerable needles. If a motion plan exists, RCS would find a motion plan in finite time assuming that the parameter resolution is fine enough, but it provides no guarantees on the motion plan cost. To achieve resolution optimality, we enhance RCS, which explores the needle’s state space in an A*-like fashion, with cost-aware duplicate pruning while incorporating motion plan cost tracking and a heuristic function to improve efficiency. We also provide a proof sketch to show the resolution optimality of our method with a careful discussion of assumptions and required conditions. We refer to our new method as RCS*, a resolution-optimal version of RCS. We also demonstrate experimentally on a realistic lung biopsy scenario that RCS* outperforms the state-of-the-art in terms of runtime and plan quality.

II. RELATED WORK

A. Motion planning for steerable needles

A variety of approaches have been proposed for the motion planning of steerable needles. Duindam et al. [15] proposed a planner based on inverse kinematics but provided no theoretical guarantees. Liu et al. [20] developed the Adaptive Fractal Tree (AFT) for needle steering. Their method iteratively refines the lowest-cost plan from the previous iteration, but refining the best plan of a coarse resolution does not necessarily lead to the best plan in a finer resolution. Pinzi et al. [21] extended it to account for goal orientation constraints.

Some planners adapt sampling-based methods such as Rapidly-exploring Random Tree (RRT) [22] for steerable needles. Xu et al. [33] used an RRT variant for needle steering but showed low time efficiency. Patil et al. [17] developed an RRT-based needle planner that samples in the 3D workspace rather than the configuration space. Sampling in a lower-dimension space and their customized distance

function made the planner work efficiently in many practical cases, but this also invalidates the probabilistic-completeness guarantee of RRT [22, 25]. To avoid dealing with curvature constraints directly, Favaro et al. [9] proposed a hybrid method to combine sampling and smoothing. First, a tree embedded in the 3D workspace is built with RRT* [26], then candidate plans found by the tree are smoothed to further account for the curvature constraint. However, such a decoupling invalidates the asymptotic optimality guarantee [26, 27]. Sun et al. [29] proposed a needle planner by building multiple RRTs, which is asymptotically optimal when the number of trees tends to infinity. Other methods focus on accounting for the uncertainty during needle insertion without providing formal guarantees [16, 18, 19].

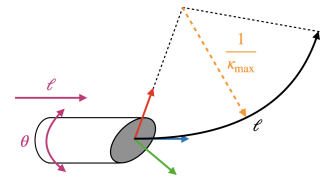
B. Resolution-optimal motion planners

Although resolution completeness has been frequently mentioned [34–38], resolution optimality earned little attention, possibly due to being rather complex to analyze mathematically, particularly for nonholonomic systems. Consequently, many planners developed for nonholonomic systems focus on asymptotic optimality instead [24, 28, 39, 40].

Barraquand et al. [35] proposed a resolution-complete planner for single or multiple robots with nonholonomic constraints. Their method is also optimal with respect to the number of reverse maneuvers in the plan. Pivtoraiko et al. [41] proposed the idea of motion planning using state lattices for field robots. Their state lattices planner is resolution optimal since the search is optimal for a graph of some resolution and the discrete state grid approximates the continuous space as resolution increases. Ljungqvist et al. [42] later extended [41] for a general two-trailer system in 2D. However, these methods are designed for large-scale workspaces, making them unsuitable for tasks where a high level of precision is required, such as for steerable needles.

III. PROBLEM DEFINITION

We consider bevel-tip flexible steerable needles [5–8] controlled by insertion and rotation at their base. A bevel-tip steerable needle is made of a highly flexible material such that, when being inserted through tissue, asymmetric forces applied by the bevel cause the needle to take a curved trajectory. The maximum curvature of the needle’s path in the tissue, κ_{\max} , is influenced by the mechanical design of the needle and the tissue that the needle moves through. Additionally, axially rotating the needle at its base changes the direction the bevel is facing, enabling us to control the steering direction. The figure to the right illustrates the needle’s kinematics, where the needle can be inserted by length ℓ and axially rotated at its base by θ .



We make the common assumption that the steerable needle is sufficiently flexible so the needle shaft moves along the

trajectory created by its tip while the lateral motions are negligible. Thus, the configuration space of the steerable needle is defined by the pose of its tip, $\mathcal{X} \subset \mathcal{SE}(3)$, where a given configuration $\mathbf{x} = (p, q) \in \mathcal{X}$, specifies the position and orientation components $p \in \mathbb{R}^3$ and $q \in \mathcal{SO}(3)$, respectively. We assume that \mathcal{X} is compact. We denote the 3D workspace by $\mathcal{W} \in \mathbb{R}^3$, a subset of which is occupied by obstacles $\mathcal{W}_{\text{obs}} \subset \mathcal{W}$. A configuration $\mathbf{x} = (p, q)$ is *collision free* if and only if $p \notin \mathcal{W}_{\text{obs}}$. We define $\mathcal{X}_{\text{free}}$ as the union of all collision-free configurations.

A motion plan of the needle is a trajectory $\sigma : [0, \ell] \rightarrow \mathcal{X}$, where ℓ is the length of the trajectory. We also use the notation ℓ_σ to denote the length of σ . A motion plan (or trajectory) σ is *collision free* if $\forall s \in [0, \ell], \sigma(s) \in \mathcal{X}_{\text{free}}$. To evaluate the quality of a motion plan, we consider a configuration-based cost function $c : \mathcal{X} \rightarrow \mathbb{R}$. We require c to be well behaved (formally defined in Sec. V), which includes being Lipschitz continuous and bounded within $[c_{\min}, c_{\max}]$. We define the cost of a motion plan as the integral of the configuration-based cost along a given trajectory σ , i.e.,

$$\mathcal{C}(\sigma) = \int_0^\ell c(\sigma(s)) ds. \quad (1)$$

This definition captures a variety of cost functions, including trajectory length and integrating over a cost map derived from medical images.

A motion plan is (kinematically) *feasible* if the curvatures along the trajectory never exceed κ_{\max} . A motion plan is *valid* if it is collision free and feasible. We are now ready to state the steerable needle motion planning problem.

Problem 1. An optimal steerable needle motion planning problem is defined as the tuple $\Delta = (\mathcal{X}, \mathcal{W}_{\text{obs}}, \mathbf{x}_{\text{start}}, p_{\text{goal}}, \tau, \ell_{\max}, \kappa_{\max}, \mathcal{C})$, where \mathcal{W}_{obs} is the obstacle set, $\mathbf{x}_{\text{start}}$ is the start configuration, $p_{\text{goal}} \in \mathcal{W}$ is the goal point, $\tau > 0$ is the goal tolerance, ℓ_{\max} is the maximum insertion length, κ_{\max} is the maximum curvature, and \mathcal{C} is a cost function. The problem calls for computing an optimal valid motion plan $\sigma^* = \operatorname{argmin}_\sigma \mathcal{C}(\sigma)$ subject to:

$$\begin{aligned} &\sigma \text{ is valid,} \\ &\sigma(0) = \mathbf{x}_{\text{start}}, \\ &\ell_\sigma \leq \ell_{\max}, \\ &\|\operatorname{Proj}(\sigma(\ell_\sigma)) - p_{\text{goal}}\|_2 \leq \tau, \end{aligned}$$

where $\operatorname{Proj}(\mathbf{x}) = p$ for $\mathbf{x} = (p, q)$.

As we show in Sec. V, for any given instance of Problem 1, under some mild assumptions, there exists a fine-enough cutoff resolution $R_{\min} = \{\delta\ell_{\min}, \delta\theta_{\min}\}$ (corresponding to the needle's insertion and axial rotation, respectively) for which our planner is guaranteed to return a motion plan with a cost to be within a desired approximation factor of a globally optimal qualified motion plan in finite time (if any qualified motion plan exists), or indicate that no qualified motion plan exists. Similar to [3], we assume there exist minimal motions that are precisely achievable by the hardware system in tissues, informing the cutoff resolution. In our specific case, the minimal motions are the minimal

Algorithm 1 RCS*

Input: $\mathcal{W}_{\text{obs}}, \mathbf{x}_{\text{start}}, p_{\text{goal}}, \tau, \kappa_{\max}, \ell_{\max}, \delta\ell_{\max}, R_{\min}$

```

1:  $\Theta \leftarrow \{0, \frac{\pi}{2}, \pi, \frac{3\pi}{2}\}, K \leftarrow \{0, \kappa_{\max}\}$ 
2:  $\text{root} \leftarrow (\mathbf{x}_{\text{start}}, 0, 0)$   $\triangleright$  The root has rank 0 and cost 0
3:  $\text{OPEN} \leftarrow \{\text{root}\}, \text{CLOSED} \leftarrow \emptyset, \text{bestPlan} \leftarrow \text{NULL}$ 
4: while not  $\text{OPEN.empty}()$  do
5:    $v \leftarrow \text{OPEN.extract}()$ 
6:   if  $\text{Valid}(v, \mathcal{W}_{\text{obs}}, p_{\text{goal}}, \ell_{\max})$  then
7:     if not  $\text{CLOSED.existDuplicate}(v)$  then
8:       if  $\text{GoalReached}(v, p_{\text{goal}}, \tau)$  then
9:          $\text{bestPlan.update}(v)$ 
10:      for  $\mathcal{M} \in \text{Primitives}(K, \delta\ell_{\max}, \Theta)$  do
11:         $\text{OPEN.insert}(v \oplus \mathcal{M})$ 
12:       $\text{CLOSED.insert}(v)$ 
13:   if  $v \neq \text{root}$  then
14:     for  $\mathcal{M} \in \text{RefinedPrimitives}(\mathcal{M}_v)$  do
15:       if  $\text{ValidResolution}(\mathcal{M}, R_{\min})$  then
16:          $\text{OPEN.insert}(v.\text{parent} \oplus \mathcal{M})$ 
17: return  $\text{bestPlan}$ 

```

insertion and minimal rotation the needle tip can precisely perform, determined by a lower-level needle controller.

IV. THE RCS* ALGORITHM

We describe our RCS* algorithm for resolution-optimal motion planning. We also highlight the differences between our new algorithm and our previous method RCS [3]. After presenting RCS*, we discuss an additional procedure to further improve its performance.

A. Algorithm description

The core idea of RCS* (and RCS) is to build a search tree with predefined motions of multiple resolutions. Specifically, RCS* constructs a search tree $\mathcal{T} = (\mathcal{V}, \mathcal{E})$ embedded in the configuration space, where each node $v \in \mathcal{V}$ is associated with a configuration $\mathbf{x}_v \in \mathcal{X}$ and each edge $e = (u, v) \in \mathcal{E}$ represents a transition from \mathbf{x}_u to \mathbf{x}_v . The search tree is rooted at the given start configuration $\mathbf{x}_{\text{start}}$ and explores valid motion plans when expanded in the configuration space. See the pseudocode of RCS* in Alg. 1.

To generate new nodes, RCS* expands existing nodes with predefined (kinematically) feasible motion primitives [43]. In RCS*, a motion primitive defines a local circular trajectory with some constant curvature $\kappa \leq \kappa_{\max}$, some length $\delta\ell > 0$, and some curving direction $\delta\theta \in [0, 2\pi)$. That is, a motion primitive is defined as a tuple $\mathcal{M} = (\kappa, \delta\ell, \delta\theta)$. We denote the operation of applying a motion primitive \mathcal{M} to configuration \mathbf{x}_v as $\mathbf{x}_u = \mathbf{x}_v \oplus \mathcal{M}$, where \mathbf{x}_u is the resultant configuration. RCS* uses a fixed set of curvatures $\{0, \kappa_{\max}\}$ and defines the resolution of a motion primitive as a function of $\delta\ell$ and $\delta\theta$, since any curvature $\kappa \in [0, \kappa_{\max}]$ can be well approximated by interleaving curvature 0 and κ_{\max} [3]. Generally speaking, the finer the resolution is, the finer the intervals $[0, \delta\ell_{\max}]$ and $[0, \delta\theta_{\max}]$ are discretized. We mention that

the coarsest resolution is set with a user-defined $\delta\ell_{\max}$ and $\delta\theta_{\max} = \pi/2$ (4 initial steering orientations as shown in line 1).

In each iteration of RCS*, an expansion of existing nodes is performed in an A*-like fashion. In particular, nodes are iteratively extracted from the OPEN list (line 5), wherein nodes are ordered according to their *rank* and a secondary metric $f(\cdot)$. We define the rank of a node as a function of the node's depth in the tree and the resolution of the motion primitives leading to the node. The deeper a node is in the tree and the finer resolution the motion primitives are, the higher rank a node has (see formal definition of rank in [3]). The secondary metric $f(v) = \mathcal{C}(v) + h(v)$ has $\mathcal{C}(v)$ denoting the cost of the trajectory from the root of \mathcal{T} to v with respect to \mathcal{C} and $h(v)$ being a heuristic function estimating the cost of the trajectory from the node v to the goal point. For example, in the case where \mathcal{C} is trajectory length, we have $h(v)$ be the length of the Dubins curve [44] on the plane spanned by \mathbf{x}_v and p_{goal} . Unlike in RCS, where nodes with lower rank are always extracted first, RCS* relaxes this ordering by introducing a *look-ahead* parameter denoted as $n_{\text{la}} \in \mathbb{N}$ (similar to the idea in [37] and [45]). At any time during the search, we denote the minimum rank of nodes in the OPEN list as r_{open} . Then we order all nodes with rank $r \leq r_{\text{open}} + n_{\text{la}}$ according to a secondary metric $f(\cdot)$. This is done to prioritize searching nodes from a coarser resolution, which speeds up finding an initial motion plan (this is similar in nature to using a focal list [46] in A*-like algorithms).

Given an extracted node v , we first check if it is valid (line 6) using the conditions described for RCS, which ensure that (i) the insertion length would not exceed ℓ_{\max} , (ii) the goal region is still reachable after getting to v , (iii) the trajectory from the root to v is not identical to another node that only needs coarser motion primitives to get to, and (iv) that the edge leading to v is collision free [3]. In addition, RCS* checks that the cost $\mathcal{C}(v)$ is smaller than the cost of the best plan reaching the goal region found so far. If the heuristic function $h(\cdot)$ is admissible, we use $f(v)$ instead of $\mathcal{C}(v)$ in the last condition, as f provides a better estimate of the node cost and hence allows to prune more vertices.

To further boost efficiency, the algorithm avoids expanding nodes that are highly similar to existing nodes in terms of the induced configuration and cost by performing duplicate detection (line 7). A node v is determined as a duplicate if there exists a node u in the CLOSED list that satisfies (i') $\rho(\mathbf{x}_u, \mathbf{x}_v) < d_{\text{sim}}$ and (ii') $\mathcal{C}(u) \leq \mathcal{C}(v)$, where ρ is a distance function defined on \mathcal{X} and d_{sim} is a similarity parameter. We use $\rho(\mathbf{x}_u, \mathbf{x}_v) = \|p_u - p_v\|_2 + \alpha \cdot \text{dist}_{\triangleleft}(q_u, q_v)$, where $\alpha > 0$ is a weighting parameter and $\text{dist}_{\triangleleft}(\cdot)$ is the angular distance between two orientations. Sec. V specifies the value of d_{sim} . Condition (i') is shared between RCS and RCS*, while condition (ii') is important for keeping RCS* resolution optimal as it prevents nodes with lower cost from being pruned away by nodes with higher cost.

RCS* uses a set of motion primitives of different resolutions, but instead of applying all motion primitives together, only the coarsest motion primitives are used when a node

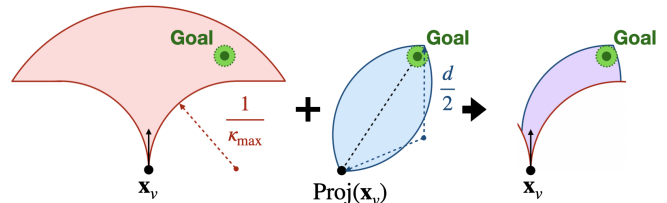


Fig. 2: A 2D illustration of the approximated reachable workspace. The kinematically forward-reachable workspace is shaded in red (a 3D version can be obtained by rotating the region around the tangent vector at \mathbf{x}_v , which results in a trumpet shape). The feasible workspace is shaded in blue. The diameter of the circular arcs is $d = \max(2/\kappa_{\max}, \tau + \|\text{Proj}(\mathbf{x}_v) - p_{\text{goal}}\|_2)$. The final approximated reachable workspace is shaded in purple.

is initially expanded (line 10). The resolution of a motion primitive (with respect to $\delta\ell$ and $\delta\theta$) is refined when a node with a coarser motion primitive is processed (line 14). More specifically, a finer motion primitive is obtained by changing $\delta\ell$ or $\delta\theta$ by a small value that corresponds to a finer resolution (see [3] for the exact definitions). Note that resolution refinement is done even if a node is invalid since finer resolutions might be valid.

Resolution refinement will be cut off when reaching a finer resolution, with respect to $\delta\ell$ or $\delta\theta$, than the predefined cutoff resolution R_{\min} (line 15). Here the cutoff resolution is determined by the minimal motions of the needle tip that are precisely achievable with the hardware system.

The algorithm terminates when the OPEN list is exhausted (line 4), and the best plan is returned (if any is found). RCS* is guaranteed to terminate in finite time due to the cutoff resolution.

B. Domain-specific optimization

We describe an additional procedure to further improve RCS*'s performance. We incorporate the concept of inevitable collisions [44] to eliminate potential nodes that would lead to collisions as they are expanded. In particular, for a given vertex v and the goal point, region growing is performed from \mathbf{x}_v within an approximated reachable workspace, considering the existence of obstacles. This region is defined as the intersection of the kinematically forward-reachable workspace and the olive-shaped feasible workspace defined by \mathbf{x}_v , p_{goal} , and tolerance τ (see Fig. 2). We mention that due to (i) maximum curvature constraint, (ii) maximum turning angle constraint (the needle would shear or buckle when turning over $\pi/2$), and (iii) maximum insertion length constraint, the kinematically forward-reachable workspace for a given needle configuration is a trumpet-shaped volume (see Fig. 2 left). In the case that the goal is not reached by the grown region, v is discarded. For additional optimizations applicable to RCS*, see Appendix A.

V. RESOLUTION OPTIMALITY OF RCS*

We study the theoretical properties of RCS* and provide a proof for the algorithm being *resolution optimal*. Informally, resolution optimality implies that RCS* is guaranteed to find a plan whose cost is as close as desired to the cost of the

globally optimal qualified motion plan σ^* , assuming that the cutoff resolution $R_{\min} = \{\delta\ell_{\min}, \delta\theta_{\min}\}$ is fine enough. Thm. 1 given below, states our main theoretical contribution relating to the resolution optimality of RCS*.

Before stating Thm. 1, we introduce the notions of a *well-behaved cost*, as well as *robust* and *decomposable* trajectories, which will be used to state the necessary conditions on \mathcal{C} and σ^* required to prove our result. The crux of the problem is that it may not be possible to approximate the optimal plan σ^* using motion plans with a finite number of transitions without additional (realistic) constraints on the cost function \mathcal{C} and on σ^* .

To this end, we start to define the notion of a *Well-behaved cost* that states that close-by configurations have similar costs and that there are bounds on the values that the cost can attain.

Definition 1 (Well-behaved cost). A configuration-based cost function c is well-behaved if (i) it is Lipschitz continuous, i.e., $\forall \mathbf{x}_1, \mathbf{x}_2 \in \mathcal{X}_{\text{free}}, |c(\mathbf{x}_1) - c(\mathbf{x}_2)| \leq L_c \cdot \rho(\mathbf{x}_1, \mathbf{x}_2)$ for $L_c \in \mathbb{R}$, and (ii) $\forall \mathbf{x} \in \mathcal{X}_{\text{free}}, c(\mathbf{x}) \in [c_{\min}, c_{\max}]$, where $c_{\min}, c_{\max} \in \mathbb{R}$ and $c_{\min} > 0$. In such a case, we also say that the trajectory-based cost function $\mathcal{C}(\sigma) = \int_0^\ell c(\sigma(s))ds$ is well-behaved.

We assume c_{\max} is not infinitely large since such configurations can be removed from $\mathcal{X}_{\text{free}}$. We also require a well-behaved cost to satisfy $c_{\min} > 0$ since in the case of needle steering, there is always a cost associated with puncturing tissue.

Next, we provide two definitions that are used to characterize motion plans that RCS* can approximate. The first definition (borrowed from [3]) is concerned with trajectories that are induced by a finite set of motion primitives (not necessarily the ones used by RCS*). The second definition is concerned with so-called robust trajectories that admit some clearance from the obstacles. A motion plan is then considered *qualified* if it satisfies both definitions.

Definition 2 (Decomposable trajectory). A trajectory $\sigma : [0, l] \rightarrow \mathcal{X}$ is decomposable if it can be decomposed into a finite set of motion primitives. Namely, there exist primitives $M_\sigma = \{\mathcal{M}_1, \dots, \mathcal{M}_n\}$ such that $\sigma = \sigma(0) \oplus M_\sigma$, where $\mathbf{x} \oplus M$ denotes the resultant trajectory obtained by sequentially applying elements in M to \mathbf{x} .

Definition 3 (Robust trajectory). A trajectory $\sigma : [0, l] \rightarrow \mathcal{X}$ is δ -robust, for some $\delta > 0$, if (i) it has δ clearance from obstacles, i.e., $\min_{s \in [0, l], \mathbf{x} \in \mathcal{X}_{\text{obs}}} \rho(\sigma(s), \mathbf{x}) > \delta$, and if (ii) its endpoint is within a distance of $\tau - \delta$ to the goal. Namely, $\|\text{Proj}(\sigma(l)) - p_{\text{goal}}\|_2 < \tau - \delta$. Here, $\mathcal{X}_{\text{obs}} = \text{cl}(\mathcal{X} \setminus \mathcal{X}_{\text{free}})$ and $\text{cl}(\cdot)$ is the closure of a set. Note that, we implicitly assume here that $\tau > \delta$.

We are ready to state our main theoretical result concerning the resolution optimality of RCS*.

Theorem 1 (Resolution optimality). *Let $\Delta = (\mathcal{X}, \mathcal{W}_{\text{obs}}, \mathbf{x}_{\text{start}}, p_{\text{goal}}, \tau, \ell_{\max}, \kappa_{\max}, \mathcal{C})$ be an optimal steerable needle motion-planning problem, $\varepsilon \in (0, \infty)$ be an*

approximation factor, and σ^ be a trajectory. Also, suppose that the following conditions are satisfied:*

- (C1) *The steerable-needle system is Lipschitz continuous and characterized with L_s (see Appendix B for formal definition);*
- (C2) *The cost function \mathcal{C} is well-behaved and characterized with L_c, c_{\min}, c_{\max} . Denote $k = \frac{L_c + c_{\max}}{c_{\min}}$.*
- (C3) *The optimal trajectory σ^* is decomposable and δ -robust with $\delta = \min\{\frac{\varepsilon}{k}, \frac{\tau}{2}\}$.*
- (C4) *The radius d_{sim} used to reject similar nodes satisfies*

$$d_{\text{sim}} < \min\left\{\frac{2}{\kappa_{\max}} \sin \frac{\kappa_{\max} \delta \ell_{\min}}{2}, \frac{\delta(L_s - 1)}{2(L_s^H - 1)}\right\}, \text{ where } H = \left\lceil \frac{\ell_{\max}}{\delta \ell_{\min}} \right\rceil.$$

Then RCS is resolution optimal, i.e., for a fine-enough cutoff resolution $R_{\min} = \{\delta\ell_{\min}, \delta\theta_{\min}\}$, RCS* will find a motion plan that satisfies $\mathcal{C}(\sigma) \leq (1 + \varepsilon) \cdot \mathcal{C}(\sigma^*)$.*

A. Proof sketch for Thm. 1

We provide a sketch of the proof for Thm. 1 and defer the full proof to Appendix B. The proof sketch consists of two main steps: We first show that the plan σ^* can be approximated by another plan σ_β^* that is composed solely of the motion primitives used by RCS*. Then, we show that even though RCS* might not be able to exactly find σ_β^* due to pruning, it will be able to recover another plan $\tilde{\sigma}_\beta^*$ whose cost is similar to that of σ_β^* (and σ^*).

We assume that the conditions in Thm. 1 are met for a plan σ^* and the approximation factor $\varepsilon > 0$. As a first step, we show that there exists a resolution R_{\min} and a trajectory σ_β^* that approximate σ^* such that σ_β^* can be constructed solely from the motion primitives of RCS*. In particular, σ_β^* is a *piece-wise strict β -approximation* of σ^* which is defined as follows: the two trajectories σ^* and σ_β^* can be partitioned into a sequence of trajectories $\sigma_1, \dots, \sigma_n$ and $\sigma'_1, \dots, \sigma'_n$, respectively, for some positive and finite integer n , such that for any $1 \leq i \leq n$ we have that (i) the Hausdorff distance between σ_i and σ'_i is below some maximal threshold $\beta > 0$, and that (ii) the cost of the two trajectories satisfies $\mathcal{C}(\sigma'_i) \leq (1 + \beta) \cdot \mathcal{C}(\sigma_i)$ (see formal definition in Appendix B). This step extends and generalizes our previous proof [3, Lemma 2] that showed the existence of such an approximation, albeit only for the length cost, and relies on assumptions **C1** and **C2**, which characterize the system and cost function, and on assumption **C3**, which states that σ^* is decomposable.

The value β is chosen to guarantee that $\mathcal{C}(\sigma_\beta^*) \leq (1 + \varepsilon) \cdot \mathcal{C}(\sigma^*)$. Moreover, the choice of β , and the fact that σ_β^* is a β -approximation of σ^* also ensure that σ_β^* is collision free and satisfies the goal tolerance according to assumption **C3**. Note that the above properties would still hold even if we replace the constant β with a slightly larger value $\beta' > \beta$. However, we use the more conservative value $\beta > 0$ to compensate for the fact that RCS* prunes the tree. In particular, due to pruning, RCS* might eliminate some of the vertices induced by the trajectory σ_β^* , and thus, we cannot guarantee that σ_β^* would be returned as a solution. However, we can show that even in the presence of pruning RCS* will compute a valid

plan $\tilde{\sigma}_\beta^*$ that tightly bounds the cost of σ_β^* (and thus tightly bounds the cost of σ^*).

We now elaborate on this. Denote the sequence of motion primitives that define σ_β^* as $M_{\sigma_\beta^*} = \{\mathcal{M}_1, \dots, \mathcal{M}_n\}$. When the motions in $M_{\sigma_\beta^*}$ are sequentially applied to $\mathbf{x}_{\text{start}}$, we obtain a sequence of configurations $\{\mathbf{x}_0, \mathbf{x}_1, \dots, \mathbf{x}_n\}$, where $\mathbf{x}_0 = \mathbf{x}_{\text{start}}$, $\mathbf{x}_i = \mathbf{x}_{i-1} \oplus \mathcal{M}_i$, $i \in [1, n]$, some of which may be pruned. By carefully bounding d_{sim} (according to **C4**), we guarantee that in the worst case the trajectory obtained by applying the same sequence of motion primitives to pruned nodes stays within a collision-free “tunnel” around σ_β^* , ensuring that it remains valid. The choice of d_{sim} also takes care of goal tolerance, guaranteeing that the trajectory still satisfies τ goal tolerance. Finally, because (i) pruning is allowed only when there exists a node with equal or smaller cost, and (ii) the subtrajectories obtained from applying the same motion primitive to close-by configurations are strict approximations, the plan $\tilde{\sigma}_\beta^*$ tightly bounds the cost of σ_β^* .

VI. RESULTS

We focus on the medical procedure of lung biopsy for evaluation. Lung and bronchus cancer has the highest death rate among all types of cancer, killing over 130,000 Americans each year [47]. Lung biopsy enables definitive diagnosis of suspicious lung nodules at an early stage, which is important to increase the survival rate. One potential approach to safely and accurately access lung nodules for biopsy and localized treatment is deploying a steerable needle trans-orally through a bronchoscope to avoid transthoracic access which could cause severe side effects [48–51]. In this approach, a physician deploys a bronchoscope through a patient’s bronchial tubes and then the steerable needle is deployed through the bronchoscope, exits out of the bronchial tube, and steers in the lung parenchyma to reach the nodule. Our motion planner focuses on the final stage of automatically steering the needle through the lung parenchyma to the nodule, while avoiding anatomical obstacles including large blood vessels, bronchial tubes, and the lung boundary.

We used the method developed in [2] to reconstruct the anatomical workspace from a chest CT scan with the above-mentioned obstacles. We collected 100 test cases. For each test case, we randomly sampled a start pose close to the bronchial tubes and a target in the lung parenchyma. We finished collecting when the number of test cases reached 100 after rejecting (i) impossible scenarios where the start pose has inevitable collision and (ii) trivial scenarios where the start pose can be connected directly to the goal point with a collision-free arc. The simulated needle has $\kappa_{\text{max}} = (50\text{mm})^{-1}$, $\ell_{\text{max}} = 100\text{mm}$, and a diameter of 2mm. We set the goal tolerance $\tau = 1.0\text{mm}$.

We compared RCS* in simulation with several planners:

- (i) **RRT**: The RRT-based needle planner [12, 17] with 5% goal biasing and 100% goal connecting ratio.
- (ii) **AO-RRT**: AO-RRT [24, 25] adapted for steerable needles, with maximum rotation control 2π and a maximum insertion control 20mm. We follow the guidelines in [25] for cost sampling and distance weighting between

the configuration space and cost space. For a fair comparison, we use the same goal connecting as RRT.

- (iii) **AFT**: The AFT-based needle planner [20, 21], with setup following [21]. AFT internally uses a hybrid cost function; we use $\mathcal{C}_{\text{hybrid}}(\sigma) = \omega \cdot \mathcal{C}(\sigma) + \|\sigma(\ell_\sigma) - p_{\text{goal}}\|_2 / \tau$, where ω is a weighting parameter depending on the scale of \mathcal{C} . Note that $\mathcal{C}_{\text{hybrid}}$ is only used internally in AFT while \mathcal{C} is always used for performance comparison across different planners.
- (iv) **RCS**: The RCS needle planner [3] with cutoff resolution $R_{\text{min}} = \{0.125\text{mm}, 0.157\text{rad}\}$, $\delta\ell_{\text{max}} = 20\text{mm}$.

RCS* used the same basic setup as RCS and $n_{\text{la}} = 3$. Additionally, for all cost functions, we set $\varepsilon = 0.1$. Since we used a CPU implementation of AFT, we did not compare its performance over time, and only reported the final cost after three iterations, as suggested in [20]. For each method, except for AFT, the timeout was set to 100 seconds. All methods except for AFT achieved 100% success rate when timed out while AFT achieved 87% success rate. When reporting the relative cost of AFT, we only consider the test cases that are successfully solved by AFT. As RRT and RCS are designed to find a plan instead of optimizing a plan, we modified them to keep running after the first plan is found, and always return the best plan found when timed out. All experiments were run on a dual 2.1GHz 16-core Intel Xeon Silver 4216 CPU and 100GB of RAM. All parallelizations were implemented with Motion Planning Templates (MPT) [52].

We used two well-behaved cost functions for which RCS* is resolution optimal: (i) trajectory length, and (ii) a cost function informed by a cost map derived from medical images [2], where each voxel in the 3D cost map is associated with a cost value that represents tissue damage. We used trilinear interpolation to smooth out the voxelized cost map and forced $c_{\text{min}} = 0.01$.

Fig. 3 shows results for the different planners for the cost map and trajectory length cost functions. For both cost functions, the cost of a plan may vary significantly between test cases. For example, trajectory length is affected by how far away the target lies relative to the start pose and cost map values are much higher when the needle is steering in a vessel-cluttered region. To account for the large variation between test cases, we first computed *relative cost* within one test case. Specifically, we took the first-found plan (no matter which method returns it as long as it is returned the fastest), and computed relative cost to this plan for all other plans found for the same test case. We did this for all the test cases, and then averaged over the 100 test cases (see the first two plots in Fig. 3). Such relative cost decreased as the result plans are gradually optimized. AFT, which is omitted from those plots, achieved a final cost of 0.574 and 0.991 for cost map and trajectory length, respectively, after three iterations.

For both cost functions, RCS* achieved the best final costs. For the cost map, which is more clinically relevant, RCS* outperformed other methods after 1.5 seconds with a final cost of 0.277, which is 50% lower than AFT (0.574), 35% lower than RRT (0.423) and AO-RRT (0.427), and

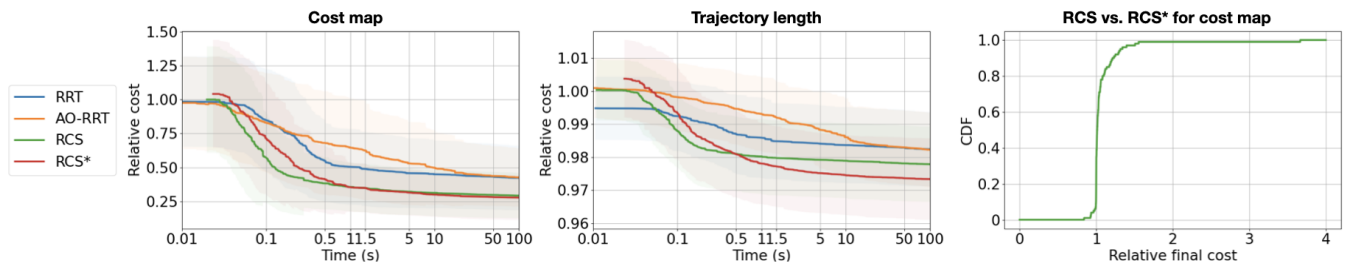


Fig. 3: **Left and middle:** Performance comparison of the different motion planning methods with two different cost functions. The time axes use a logarithmic scale. The shaded regions show standard deviations. **Right:** A detailed comparison of RCS and RCS* for the cost-map setting, shown as a cumulative distribution function (CDF).

7% lower than RCS (0.299). This indicates that the final plan produced by RCS* successfully avoids more small blood vessels than the other methods. It is worth mentioning that unlike trajectory length, small perturbations may lead to very different costs when we use the cost map. As for trajectory length, all methods generated trajectories with roughly similar lengths, although RCS* computed shorter trajectories than all other methods.

In Fig. 3, we report the cumulative distribution function across the 100 test cases of the relative final cost of RCS with respect to RCS* for the cost-map setting. Although RCS achieved comparable costs with RCS* in most cases, for about 20% of the test cases RCS achieved a motion plan that is at least 10% more costly than RCS*. In the extreme case, the final cost of RCS was 3.67 times that of RCS*.

Finally, we mention that the number of nodes RCS* explored is only 53% (for cost map) and 30% (for trajectory length) of that RCS explored. This indicates that although RCS* spent more time choosing the right node to explore, it explores much fewer nodes than RCS to get a plan with even higher quality. The experimental results demonstrate that RCS* is faster than competing methods and that the theoretical guarantees of RCS* have a practical impact on the quality of result plans, which is valuable for computing motion plans that minimize patient trauma.

VII. CONCLUSION

In this paper, we introduce the first resolution-optimal motion planner for steerable needles. In particular, our method returns in finite time a motion plan whose cost can be as close as desired to the globally optimal qualified motion plan, assuming the given resolution is fine enough. We also provide a proof sketch to show the resolution optimality of our method with a careful discussion of assumptions and required conditions. We evaluate our proposed planner with simulation experiments and show it can efficiently compute high-quality motion plans considering clinically relevant cost functions. In the future, we plan to investigate speedup techniques for vertex validation and pruning to reduce vertex expansion time. In addition, we plan to develop explicit expressions for the resolution R_{\min} necessary to achieve the desired level of approximation quality for a given problem instance. We will also experimentally evaluate the planner with steerable needles in ex-vivo tissues.

REFERENCES

- [1] M. Fu, K. Solovey, O. Salzman, and R. Alterovitz, “steerable-needle-planner,” <https://github.com/UNC-Robotics/steerable-needle-planner>, 2021, accessed: 2022-02-15.
- [2] M. Fu, A. Kuntz, R. J. Webster III, and R. Alterovitz, “Safe motion planning for steerable needles using cost maps automatically extracted from pulmonary images,” in *IEEE/RSJ Int. Conf. Intelligent Robots and Systems (IROS)*. IEEE, 2018, pp. 4942–4949.
- [3] M. Fu, O. Salzman, and R. Alterovitz, “Toward Certifiable Motion Planning for Medical Steerable Needles,” in *Proceedings of Robotics: Science and Systems*, Virtual, July 2021.
- [4] N. Abolhassani, R. Patel, and M. Moallem, “Needle insertion into soft tissue: A survey,” *Medical Engineering & Physics*, vol. 29, no. 4, pp. 413–431, 2007.
- [5] R. Alterovitz, K. Goldberg, and A. Okamura, “Planning for steerable bevel-tip needle insertion through 2D soft tissue with obstacles,” in *IEEE Int. Conf. Robotics and Automation (ICRA)*. IEEE, 2005, pp. 1640–1645.
- [6] N. J. Cowan, K. Goldberg, G. S. Chirikjian, G. Fichtinger, R. Alterovitz, K. B. Reed, V. Kalleem, W. Park, S. Misra, and A. M. Okamura, “Robotic needle steering: design, modeling, planning, and image guidance,” in *Surgical Robotics: System Applications and Visions*, J. Rosen, B. Hannaford, and R. M. Satava, Eds. Springer, 2011, ch. 23, pp. 557–582.
- [7] W. Park, J. S. Kim, Y. Zhou, N. J. Cowan, A. M. Okamura, and G. S. Chirikjian, “Diffusion-based motion planning for a nonholonomic flexible needle model,” in *Proc. IEEE Int. Conf. Robotics and Automation (ICRA)*, Apr. 2005, pp. 4611–4616.
- [8] R. J. Webster III, J. S. Kim, N. J. Cowan, G. S. Chirikjian, and A. M. Okamura, “Nonholonomic modeling of needle steering,” *Int. J. Robotics Research (IJRR)*, vol. 25, no. 5-6, pp. 509–525, 2006.
- [9] A. Favaro, L. Cerri, S. Galvan, F. Rodriguez y Baena, and E. De Momi, “Automatic optimized 3D path planner for steerable catheters with heuristic search and uncertainty tolerance,” in *IEEE Int. Conf. Robotics and Automation (ICRA)*. IEEE, 2018, pp. 9–16.
- [10] R. Wein, J. Van Den Berg, and D. Halperin, “Planning high-quality paths and corridors amidst obstacles,” *Int. J. Robotics Research (IJRR)*, vol. 27, no. 11-12, pp. 1213–1231, 2008.
- [11] P. K. Agarwal, K. Fox, and O. Salzman, “An efficient algorithm for computing high-quality paths amid polygonal obstacles,” *ACM Transactions on Algorithms (TALG)*, vol. 14, no. 4, pp. 1–21, 2018.
- [12] A. Kuntz, L. G. Torres, R. H. Feins, R. J. Webster III, and R. Alterovitz, “Motion planning for a three-stage multilumen transoral lung access system,” in *IEEE/RSJ Int. Conf. Intelligent Robots and Systems (IROS)*. IEEE, 2015, pp. 3255–3261.
- [13] M. P. Strub and J. D. Gammell, “Admissible heuristics for obstacle clearance optimization objectives,” *arXiv preprint arXiv:2104.02298v2 [cs.RO]*, 2021.
- [14] M. Bentley, C. Rucker, C. Reddy, O. Salzman, and A. Kuntz, “A novel shaft-to-tissue force model for safer motion planning of steerable needles,” *CoRR*, vol. abs/2101.02246, 2021.
- [15] V. Duindam, J. Xu, R. Alterovitz, S. Sastry, and K. Goldberg, “Three-dimensional motion planning algorithms for steerable needles using inverse kinematics,” *Int. J. Robotics Research (IJRR)*, vol. 29, no. 7, pp. 789–800, 2010.
- [16] K. Hauser, R. Alterovitz, N. Chentanez, A. Okamura, and K. Goldberg, “Feedback control for steering needles through 3D deformable tissue

- using helical paths,” in *Proceedings of Robotics: Science and Systems*, Seattle, USA, June 2009.
- [17] S. Patil, J. Burgner, R. J. Webster III, and R. Alterovitz, “Needle steering in 3D via rapid replanning,” *IEEE Trans. Robotics*, vol. 30, no. 4, pp. 853–864, 2014.
- [18] K. M. Seiler, S. P. Singh, S. Sukkarieh, and H. Durrant-Whyte, “Using Lie group symmetries for fast corrective motion planning,” *Int. J. Robotics Research (IJRR)*, vol. 31, no. 2, pp. 151–166, 2012.
- [19] J. Van Den Berg, S. Patil, R. Alterovitz, P. Abbeel, and K. Goldberg, “LQG-based planning, sensing, and control of steerable needles,” in *Workshop on the Algorithmic Foundations of Robotics (WAFR)*. Springer, 2010, pp. 373–389.
- [20] F. Liu, A. Garriga-Casanovas, R. Secoli, and F. Rodriguez y Baena, “Fast and adaptive fractal tree-based path planning for programmable bevel tip steerable needles,” *IEEE Robotics and Automation Letters*, vol. 1, no. 2, pp. 601–608, 2016.
- [21] M. Pinzi, S. Galvan, and F. Rodriguez y Baena, “The adaptive hermite fractal tree (AHFT): a novel surgical 3D path planning approach with curvature and heading constraints,” *Int. J. Computer Assisted Radiology and Surgery*, vol. 14, no. 4, pp. 659–670, 2019.
- [22] S. M. LaValle and J. J. K. Jr., “Randomized kinodynamic planning,” *Int. J. Robotics Res.*, vol. 20, no. 5, pp. 378–400, 2001.
- [23] M. Kleinbort, K. Solovey, Z. Littlefield, K. E. Bekris, and D. Halperin, “Probabilistic completeness of RRT for geometric and kinodynamic planning with forward propagation,” *IEEE Robotics and Automation Letters*, vol. 4, no. 2, pp. x–xvi, 2018.
- [24] K. Hauser and Y. Zhou, “Asymptotically optimal planning by feasible kinodynamic planning in a state–cost space,” *IEEE Trans. Robotics*, vol. 32, no. 6, pp. 1431–1443, 2016.
- [25] M. Kleinbort, E. Granados, K. Solovey, R. Bonalli, K. E. Bekris, and D. Halperin, “Refined analysis of asymptotically-optimal kinodynamic planning in the state-cost space,” in *IEEE Int. Conf. Robotics and Automation (ICRA)*. IEEE, 2020, pp. 6344–6350.
- [26] S. Karaman and E. Frazzoli, “Sampling-based algorithms for optimal motion planning,” *Int. J. Robotics Research (IJRR)*, vol. 30, no. 7, pp. 846–894, 2011.
- [27] K. Solovey, L. Janson, E. Schmerling, E. Frazzoli, and M. Pavone, “Revisiting the asymptotic optimality of RRT*,” in *IEEE International Conference on Robotics and Automation (ICRA)*, 2020, pp. 2189–2195.
- [28] Y. Li, Z. Littlefield, and K. E. Bekris, “Asymptotically optimal sampling-based kinodynamic planning,” *Int. J. Robotics Research (IJRR)*, vol. 35, no. 5, pp. 528–564, 2016.
- [29] W. Sun, S. Patil, and R. Alterovitz, “High-frequency replanning under uncertainty using parallel sampling-based motion planning,” *IEEE Trans. Robotics*, vol. 31, no. 1, pp. 104–116, 2015.
- [30] O. Salzman and D. Halperin, “Asymptotically-optimal motion planning using lower bounds on cost,” in *IEEE Int. Conf. Robotics and Automation (ICRA)*, 2015, pp. 4167–4172.
- [31] M. Tsao, K. Solovey, and M. Pavone, “Sample complexity of probabilistic roadmaps via ϵ -nets,” in *International Conference on Robotics and Automation*. IEEE, 2020, pp. 2196–2202.
- [32] D. Dayan, K. Solovey, M. Pavone, and D. Halperin, “Near-optimal multi-robot motion planning with finite sampling,” in *IEEE International Conference on Robotics and Automation*, 2021.
- [33] J. Xu, V. Duindam, R. Alterovitz, and K. Goldberg, “Motion planning for steerable needles in 3D environments with obstacles using rapidly-exploring random trees and backchaining,” in *IEEE Int. Conf. Automation Science and Engineering*. IEEE, 2008, pp. 41–46.
- [34] J. Barraquand and J.-C. Latombe, “Robot motion planning: A distributed representation approach,” *Int. J. Robotics Research (IJRR)*, vol. 10, no. 6, pp. 628–649, 1991.
- [35] —, “Nonholonomic multibody mobile robots: Controllability and motion planning in the presence of obstacles,” *Algorithmica*, vol. 10, no. 2, pp. 121–155, 1993.
- [36] P. Cheng and S. M. LaValle, “Resolution complete rapidly-exploring random trees,” in *IEEE Int. Conf. Robotics and Automation (ICRA)*, vol. 1. IEEE, 2002, pp. 267–272.
- [37] S. R. Lindemann and S. M. LaValle, “Multiresolution approach for motion planning under differential constraints,” in *IEEE Int. Conf. Robotics and Automation (ICRA)*. IEEE, 2006, pp. 139–144.
- [38] D. S. Yershov and S. M. LaValle, “Sufficient conditions for the existence of resolution complete planning algorithms,” in *Workshop on the Algorithmic Foundations of Robotics (WAFR)*. Springer, 2010, pp. 303–320.
- [39] J. D. Gammell and M. P. Strub, “Asymptotically optimal sampling-based motion planning methods,” *Annual Review of Control, Robotics, and Autonomous Systems*, vol. 4, pp. 295–318, 2021.
- [40] R. Shome and L. E. Kavraki, “Asymptotically optimal kinodynamic planning using bundles of edges,” in *IEEE Int. Conf. Robotics and Automation (ICRA)*, vol. 30, 2021.
- [41] M. Pivtoraiko, R. A. Knepper, and A. Kelly, “Differentially constrained mobile robot motion planning in state lattices,” *Journal of Field Robotics*, vol. 26, no. 3, pp. 308–333, 2009.
- [42] O. Ljungqvist, N. Evestedt, M. Cirillo, D. Axehill, and O. Holmer, “Lattice-based motion planning for a general 2-trailer system,” in *IEEE Intelligent Vehicles Symposium (IV)*. IEEE, 2017, pp. 819–824.
- [43] E. Frazzoli, M. A. Dahleh, and E. Feron, “Real-time motion planning for agile autonomous vehicles,” *Journal of Guidance, Control, and Dynamics*, vol. 25, no. 1, pp. 116–129, 2002.
- [44] S. M. LaValle, *Planning algorithms*. Cambridge university press, 2006.
- [45] A. Mandalika, O. Salzman, and S. S. Srinivasa, “Lazy receding horizon A* for efficient path planning in graphs with expensive-to-evaluate edges,” in *Int. Conf. Automated Planning and Scheduling (ICAPS)*, 2018, pp. 476–484.
- [46] J. Pearl and J. H. Kim, “Studies in semi-admissible heuristics,” *IEEE Trans. Pattern Anal. Mach. Intell.*, no. 4, pp. 392–399, 1982.
- [47] R. L. Siegel, K. D. Miller, H. E. Fuchs, and A. Jemal, “Cancer statistics, 2022,” *CA: a cancer journal for clinicians*, 2022.
- [48] A. Kuntz, P. J. Swaney, A. Mahoney, R. H. Feins, Y. Z. Lee, R. J. Webster III, and R. Alterovitz, “Toward transoral peripheral lung access: Steering bronchoscope-deployed needles through porcine lung tissue,” in *Hamlyn Symposium on Medical Robotics*, 2016, pp. 9–10.
- [49] P. J. Swaney, A. W. Mahoney, B. I. Hartley, A. A. Ramirez, E. Lamers, R. H. Feins, R. Alterovitz, and R. J. Webster III, “Toward transoral peripheral lung access: Combining continuum robots and steerable needles,” *Journal of Medical Robotics Research*, vol. 2, no. 01, p. 1750001, 2017.
- [50] J. Hoelscher, M. Fu, I. Fried, M. Emerson, T. E. Ertop, M. Rox, A. Kuntz, J. A. Akulian, R. J. Webster III, and R. Alterovitz, “Backward planning for a multi-stage steerable needle lung robot,” *IEEE Robotics and Automation Letters*, vol. 6, no. 2, pp. 3987–3994, 2021.
- [51] I. Fried, J. Hoelscher, M. Fu, M. Emerson, T. E. Ertop, M. Rox, J. Granna, A. Kuntz, J. A. Akulian, R. J. Webster III, and R. Alterovitz, “Design considerations for a steerable needle robot to maximize reachable lung volume,” in *IEEE Int. Conf. Robotics and Automation (ICRA)*. IEEE, 2021.
- [52] J. Ichnowski and R. Alterovitz, “Motion planning templates: A motion planning framework for robots with low-power CPUs,” in *IEEE Int. Conf. Robotics and Automation (ICRA)*. IEEE, 2019, pp. 612–618.
- [53] D. S. Minhas, J. A. Engh, M. M. Fenske, and C. N. Riviere, “Modeling of needle steering via duty-cycled spinning,” in *Annual International Conference of the IEEE Engineering in Medicine and Biology Society (EMBC)*. IEEE, 2007, pp. 2756–2759.

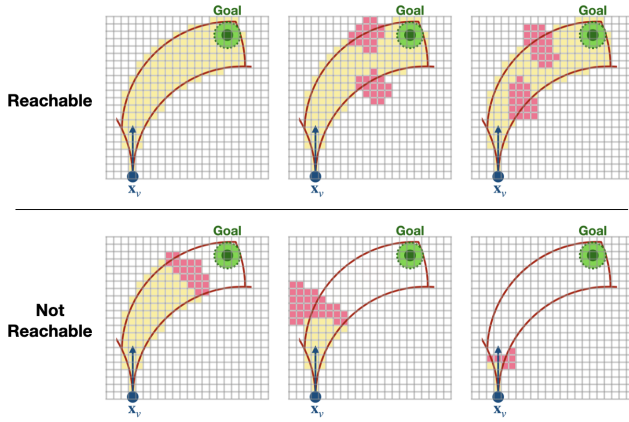


Fig. A: 2D illustration of example cases for inevitable collision check. The connected region is shaded yellow, obstacle voxels are shaded pink. This is an over estimation so even if the goal is determined as reachable in the check, it is not guaranteed that a valid motion plan to the goal exists.

APPENDIX A. DOMAIN-SPECIFIC OPTIMIZATIONS

We describe additional domain-specific optimizations to further improve RCS^{*}'s performance.

First we elaborate on the a method accounting for inevitable collisions [44] to eliminate potential nodes that are bound to lead to collisions as they are expanded, that we briefly described in Sec. IV-B. In particular, for a given vertex v and the goal point, a “region-growing” process is performed from \mathbf{x}_v within an approximation of the reachable workspace, while considering the existence of obstacles. This region is defined as the intersection of the kinematically forward-reachable workspace and the olive-shaped feasible workspace defined by \mathbf{x}_v , p_{goal} , and tolerance τ (see Fig. 2).

We mention that due to (i) maximum curvature constraint, (ii) maximum turning angle constraint (the needle would shear or buckle when turning over $\pi/2$), and (iii) maximum insertion length constraint, the kinematically forward-reachable workspace for a given needle configuration is a trumpet-shaped volume rooted at the current needle position (see Fig. 2 left).

Additionally, a position in the workspace is potentially feasible only when there exists some orientation with which the goal region is forward reachable while the start point is backward reachable, considering the maximum curvature constraint. This defines the olive-shaped feasible workspace (see Fig. 2 middle) since for any position outside the region, there is no orientation that is valid.

In the case that the goal is not reached by the grown region, v is discarded. Several examples are provided in Fig. A. Inevitable collision check allows us to efficiently identify and discard invalid branches without refining the resolution.

In addition to the above-mentioned optimization, all domain-specific optimizations introduced for RCS [3] are also applicable to RCS^{*}. More specifically, the optimizations are as follows. (i) Early pruning by testing for goal reachability. I.e., we check if the goal region overlaps with the kinematically forward-reachable workspace for a config-

uration. (ii) Direct goal connection. I.e., we try connecting a configuration to the goal point with a kinematically-feasible trajectory, and a plan is found if the trajectory is collision free. In RCS, a circular arc with constant curvature is used while in RCS^{*}, we use the trajectory with the shortest length, which is the Dubins curve [44]. (iii) Equivalent node pruning. I.e., we avoid duplicated nodes caused by refining $\delta\ell$ and $\delta\theta$ in a different order. (iv) Parallelism. I.e., we process multiple nodes in parallel to improve the overall runtime. Refer to [3] for more details.

APPENDIX B. FULL PROOF FOR THE RESOLUTION OPTIMALITY OF RCS^{*}

We provide a full proof of Theorem 1, which states that RCS^{*} is resolution optimal. Our proof below follows the proof sketch we provided in Section V. We start this section by providing some definitions that were omitted in the proof sketch. We then establish a basic property stating that decomposable trajectories can be approximated by a finite sequence of motion primitives. We then exploit this property in the full proof of Thm. 1.

A. Preliminaries

We provide a formal definition of the notion of piece-wise strict β -approximation, which we briefly described in the proof sketch. We first define this notion for a single local “piece” in the following definition, and then extend it for trajectories consisting of several pieces.

Definition 4 (Local strict approximation). For two trajectories $\sigma : [0, l] \rightarrow \mathcal{X}$ and $\sigma' : [0, l'] \rightarrow \mathcal{X}$, and a value $\beta > 0$, we say σ' is a local strict β -approximation of σ if

- (i) $l' \leq (1 + \beta) \cdot l$,
- (ii) $\forall s \in [0, \min(l, l')], \rho(\sigma(s), \sigma'(s)) \leq \beta$,
- (iii) $\forall s \in [\min(l, l'), l'], \rho(\sigma(l), \sigma'(s)) \leq \beta$.

Note that this definition is stricter than bounding the two-way Hausdorff distance between two trajectories since it requires bounded trajectory length and bounded distances between corresponding points on the trajectories. This is a major difference from our previous definition [3], where we used non-strict approximations. This will be an important tool for bounding the cost of the trajectory computed by RCS^{*}. Next, we extend this notion to multiple pieces.

Definition 5 (Piece-wise strict approximation). For two trajectories $\sigma : [0, l] \rightarrow \mathcal{X}$ and $\sigma' : [0, l'] \rightarrow \mathcal{X}$, and a value $\beta > 0$, we say σ' is a piece-wise strict β -approximation of σ if there exists two sequences $\{s_0, s_1, \dots, s_n\}$ and $\{s'_0, s'_1, \dots, s'_n\}$ that

- (i) $s_0 = 0, s'_0 = 0$,
- (ii) $s_n = l, s'_n = l'$, and
- (iii) $\forall i \in [0, n - 1]$, the sub-trajectory $\sigma'(s'_i, s'_{i+1})$ is a local strict β -approximation of $\sigma(s_i, s_{i+1})$.

Next, we provide a formal definition of Lipschitz continuity of the steerable-needle system, which is used in (C1) of Thm. 1. Following [3], we define the action space (or motion space) $\mathcal{A} \in \mathbb{R}^3$ to be the set of all feasible motion

primitives. A motion primitive $\mathcal{M} = (\kappa, \delta\ell, \delta\theta)$ is feasible if $\kappa \in [0, \kappa_{\max}]$, $\delta\ell > 0$, $\delta\theta \in [0, 2\pi)$. We then define Lipschitz continuity in our primitive-based setting, which is based on the following primitive-based metric.

Definition 6 (Primitive-based metric $\rho_{\mathcal{A}}$). We define a distance metric on an action space \mathcal{A} as a distance between two resultant trajectories from applying \mathcal{M}_1 and \mathcal{M}_2 to \mathbf{x} , where $\mathcal{M}_1, \mathcal{M}_2 \in \mathcal{A}$ and $\mathbf{x} \in \mathcal{X}$. Formally, we have

$$\begin{aligned} \rho_{\mathcal{A}}(\mathcal{M}_1, \mathcal{M}_2) &:= \max \left\{ \max_{s \in [0, l_{\min})} \rho(\sigma_{\mathcal{M}_1}(s), \sigma_{\mathcal{M}_2}(s)), \right. \\ &\quad \left. \max_{s \in [l_{\min}, l_{\max}]} \rho(\sigma_{\mathcal{M}_1}(\min\{s, l_1\}), \sigma_{\mathcal{M}_2}(\min\{s, l_2\})) \right\}, \end{aligned}$$

where $\sigma_{\mathcal{M}_1}, \sigma_{\mathcal{M}_2}$ are the resultant trajectories, l_1, l_2 are the trajectory length of $\sigma_{\mathcal{M}_1}$ and $\sigma_{\mathcal{M}_2}$, respectively, $l_{\min} = \min\{l_1, l_2\}$, and $l_{\max} = \max\{l_1, l_2\}$.

In the above definition note that changing the initial configuration \mathbf{x} does not change the relative position between the two trajectories. Thus, without loss of generality, we have $\mathbf{x} = (p, q)$ where $p = (0, 0, 0)$ and $q = (1, 0, 0, 0)$.

Definition 7 (Lipschitz continuous). The system is Lipschitz continuous if for any $\mathbf{x}_1, \mathbf{x}_2 \in \mathcal{X}$, $\mathcal{M}_1, \mathcal{M}_2 \in \mathcal{A}$, it holds that

$$\rho(\mathbf{x}_1 \oplus \mathcal{M}_1, \mathbf{x}_2 \oplus \mathcal{M}_2) \leq L_s (\rho(\mathbf{x}_1, \mathbf{x}_2) + \rho_{\mathcal{A}}(\mathcal{M}_1, \mathcal{M}_2)),$$

for some constant $L_s > 0$.

Finally, we introduce the notion of the *finest set* of motion primitives.

Definition 8 (Finest set of motion primitives). Given a resolution $R = \{r_\ell, r_\theta\}$, and a set of curvatures K , we define the *finest set of motion primitives* as

$$M_{\text{fs}}(R, K) = \left\{ (\kappa, r_\ell, n \cdot r_\theta) \mid \kappa \in K, n \in \left[0, \left\lfloor \frac{2\pi}{r_\theta} \right\rfloor \right] \subset \mathbb{Z} \right\}.$$

B. Approximation of decomposable trajectories

We temporarily set aside the study of RCS*'s behavior. We prove the following basic result showing that any decomposable trajectory can be approximated to any desirable degree by a finite sequence of motion primitives.

Theorem 2. *Let σ be a decomposable trajectory and let $\beta > 0$ be some real value. If the system is Lipschitz continuous, there exists a fine resolution $R(\sigma, \beta) = \{r_\ell, r_\theta\}$ and a finite sequence of motion primitives $M_{R(\sigma, \beta)} \subseteq M_{\text{fs}}(R(\sigma, \beta), \{0, \kappa_{\max}\})$ such that $\sigma' := \sigma(0) \oplus M_{R(\sigma, \beta)}$ is a piece-wise strict β -approximation of σ . Moreover, if c is a well-behaved cost (characterized with L_c, c_{\min}, c_{\max}), then the trajectory cost satisfies $\mathcal{C}(\sigma') \leq (1 + k \cdot \beta) \cdot \mathcal{C}(\sigma)$, where $k = \frac{L_c + c_{\max}}{c_{\min}}$.*

We break the proof of this result into the following steps.

1) *Approximating curves with arbitrary curvatures:* As a first step towards proving Thm. 2, we show that a trajectory σ as in Thm. 2, which has arbitrary curvature, can be approximated by a finite sequence of motion primitives whose

curvature is either 0 or κ_{\max} . We provide a justification of this property below.

When a bevel-tip needle is inserted only, it follows a trajectory with curvature κ_{\max} . When the needle is inserted while applying axial rotational velocity that is relatively larger than the insertion velocity, it follows a straight line (i.e., of curvature zero). Minhas et al. [53] introduced the notion of duty-cycling to approximate any curvature by bevel-tip steerable needles. Roughly speaking, combining periods of needle spinning (i.e., zero-curvature trajectories) with periods of non-spinning (i.e., maximal-curvature trajectories) enables the needle to achieve any curvature up to the maximum needle curvature. This idea is formalized in the following lemma.

Lemma 1 (Arbitrary curvature approximation using duty-cycling). *Let σ be a decomposable trajectory and let $\beta_d > 0$ be some real value. There exists a finite sequence of motion primitives M_D in which every element has curvature $\kappa \in \{0, \kappa_{\max}\}$ such that the trajectory $\sigma(0) \oplus M_D$ is a piece-wise strict β_d -approximation of σ .*

Proof Sketch. In order to make the connection the approximation factor explicit we provide a proof from a geometric perspective (and not control-based as in the original work by Minhas et al. [53]).

As the trajectory σ is decomposable, there exists a sequence of motion primitives $M_\sigma = \{\mathcal{M}_1, \dots, \mathcal{M}_n\}$ such that $\sigma = \sigma(0) \oplus M_\sigma$ and each motion primitive \mathcal{M}_i has arbitrary curvature $\kappa_i \in [0, \kappa_{\max}]$. To approximate \mathcal{M}_i , we construct a sequence of motion primitives $M_i = \{\mathcal{M}_i^{(1)}, \dots, \mathcal{M}_i^{(n_i)}\}$ that satisfies

$$\begin{aligned} \mathcal{M}_i^{(1)} \cdot \delta\theta &= \mathcal{M}_i \cdot \delta\theta, \\ \forall j \in [2, n_i], \mathcal{M}_i^{(j)} \cdot \delta\theta &= 0, \\ \forall j \in [1, n_i], \mathcal{M}_i^{(j)} \cdot \kappa &\in \{0, \kappa_{\max}\}. \end{aligned}$$

Namely, the first motion primitive $\mathcal{M}_i^{(1)}$ ensures that both trajectories use the same curving plane and the the rest of the sequence stays within this curving plane and approximates the (arbitrary) curvature κ_i .

We then decompose \mathcal{M}_i into small equal-length segments of length ℓ_i (except possibly the last segment) where the specific value of ℓ_i is chosen according to the value of β_d . We then use three motion primitives to approximate each of these segments as illustrated in Fig. B. Note that (i) the start and end configurations of \mathcal{M}_i and M_i are identical, (ii) the two-way Hausdorff distance between \mathcal{M}_i and each $\mathcal{M}_i^{(j)}$ is less than β'_d if ℓ_i is carefully chosen, and (iii) for each segment with length ℓ_i , the length of the three-segment approximation is less than $(1 + \beta'_d) \cdot \ell_i$ if ℓ_i is carefully chosen. By carefully choosing β'_d , we then can make sure the three-segment approximation is a strict β_d -approximation of the original segment, where $\beta'_d \leq \beta_d$.

Let $M_\sigma^{\beta_d} = M_1 \cdot M_2 \cdot \dots \cdot M_n$ be this sequence of all the newly constructed motion primitives. Then it is straightforward that $\sigma(0) \oplus M_\sigma^{\beta_d}$ is a piece-wise strict β_d -approximation of σ . \square

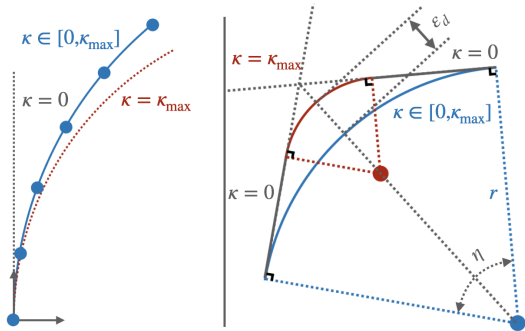


Fig. B: **Illustration of approximation with duty-cycling.** **Left:** Decompose \mathcal{M}_i into multiple segments with length ℓ_i . **Right:** Use three segments to approximate one segment of \mathcal{M}_i , where the segments have a curvature of 0, κ_{\max} and 0, respectively. The two-way Hausdorff distance (the positional part marked as ε_d in the figure) depends on ℓ_i . For a given κ_{\max} , to approximate \mathcal{M}_i (with curvature κ), the shorter ℓ_i is, the smaller ε_d is. This is because $\varepsilon_d < r \cdot (1/\cos(0.5\eta) - 1)$, where $r = 1/\kappa$ is the radius of curvature and $\eta = \ell_i/r$ is the central angle. Since maximum orientation difference along the trajectory is bounded by 0.5η , the two-way Hausdorff distance in configuration space is also bounded. Also, the trajectory length of the original segment is $r \cdot \eta + \alpha \cdot \eta$, and the length of the three-segment trajectory is $\ell_{\text{approx}} \leq 2r \cdot \tan(0.5\eta) + \alpha \cdot \eta$. Since $\lim_{\eta \rightarrow 0} 2 \cdot \tan(0.5\eta)/\eta = 1$, the trajectory length ratio approaches 1 when η approaches 0. This means the trajectory length can be approximated arbitrarily well.

2) *Approximating curves using fixed-resolution primitives:* Next, we refine Lem. 1 by showing σ can be approximated by fixed-resolution primitives.

Lemma 2 (Fixed-resolution trajectory approximation). *Let σ be a decomposable trajectory and let $\beta_r > 0$ be some real value. If the system is Lipschitz continuous (Def. 7), there exists a fine resolution $R(\sigma, \beta_r) = \{r_\ell, r_\theta\}$ and a finite sequence of motion primitives $M_{R(\sigma, \beta_r)}$ such that $\sigma(0) \oplus M_{R(\sigma, \beta_r)}$ is a piece-wise strict β_r -approximation of σ . Moreover $M_{R(\sigma, \beta_r)} \subseteq \mathcal{M}_{\text{fs}}(R(\sigma, \beta_r), K_\sigma)$, where K_σ is the set of curvatures that appear along σ .*

Proof Sketch. The following is adapted from [34, Appendix A]). The trajectory σ is decomposable, thus there exists a finite sequence of motion primitives $M_\sigma = \{\mathcal{M}_1, \dots, \mathcal{M}_n\}$ such that $\sigma = \sigma(0) \oplus M_\sigma$. Set $K_\sigma = \bigcup_i \mathcal{M}_i \cdot \kappa$ to be the set of all curvatures that appear in M_σ .

To approximate each motion primitive \mathcal{M}_i using primitives from the finest set of motion primitives $\mathcal{M}_{\text{fs}}(R(\sigma, \beta_r), K_\sigma)$ (Def. 8), we construct a sequence motion primitive $M_i = \{\mathcal{M}_i^{(1)}, \dots, \mathcal{M}_i^{(n_i)}\}$, where

$$\begin{aligned} \mathcal{M}_i^{(1)} \cdot \delta\theta &= k_i \cdot r_\theta, \\ \forall j \in [2, n_i], \mathcal{M}_i^{(j)} \cdot \delta\theta &= 0, \\ \forall j \in [1, n_i], \mathcal{M}_i^{(j)} \cdot \kappa &= \mathcal{M}_i \cdot \kappa, \mathcal{M}_i^{(j)} \cdot \delta\ell = r_\ell. \end{aligned}$$

Similar to the sequence constructed for Lem. 1, the first motion primitive $\mathcal{M}_i^{(1)}$ accounts for the curving plane (though here it can only be approximated) and the rest of the sequence stays within this curving plane and accounts for the length of the circular arc the trajectory follows in this plane. Applying the sequence M_i is equivalent to applying one motion primitive $\tilde{\mathcal{M}}_i = (\mathcal{M}_i \cdot \kappa, n_i \cdot r_\ell, k_i \cdot r_\theta)$. Thus, by

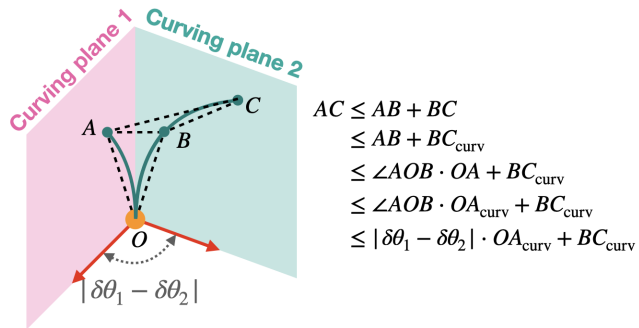


Fig. C: Illustration of the action distance between two motion primitives with the same curvature. Here the shorter motion primitive lies in curving plane 1, thus $\min\{\delta\ell_1, \delta\ell_2\} = OA_{\text{curv}}$ and $|\delta\ell_1 - \delta\ell_2| = OC_{\text{curv}} - OA_{\text{curv}} = BC_{\text{curv}}$.

carefully choosing r_ℓ and r_θ , the distance between \mathcal{M}_i and $\tilde{\mathcal{M}}_i$ (see Def. 6) can be arbitrarily small.

This is done for every motion primitive \mathcal{M}_i . As M is a finite sequence of size n , for any $\varepsilon > 0$ we can always find a fine-enough resolution $\{r_\ell, r_\theta\}$ that ensures that

$$\rho_{\mathcal{A}}(\mathcal{M}_i, \tilde{\mathcal{M}}_i) < \varepsilon, \forall i \in [1, n].$$

This is because, given that both motion primitives have equal curvature, $\rho_{\mathcal{A}}(\mathcal{M}_1, \mathcal{M}_2) < |\delta\theta_1 - \delta\theta_2| \cdot \min\{\delta\ell_1, \delta\ell_2\} + |\delta\ell_1 - \delta\ell_2| + \alpha(|\delta\theta_1 - \delta\theta_2| + \frac{|\delta\ell_1 - \delta\ell_2|}{\mathcal{M}_i \cdot \kappa})$, where $\delta\ell_i = \mathcal{M}_i \cdot \delta\ell$ and $\delta\theta_i = \mathcal{M}_i \cdot \delta\theta$. The above upper bound for the action-space distance accounts for both position and orientation. See Fig. C for illustration.

Since the system is Lipschitz continuous,

$$\begin{aligned} &\rho(\sigma(0) \oplus \mathcal{M}_1 \cdots \oplus \mathcal{M}_n, \sigma(0) \oplus \tilde{\mathcal{M}}_1 \cdots \oplus \tilde{\mathcal{M}}_n) \\ &\leq L_s(\rho(\sigma(0) \oplus \mathcal{M}_1 \cdots \oplus \mathcal{M}_{n-1}, \sigma(0) \oplus \tilde{\mathcal{M}}_1 \cdots \oplus \tilde{\mathcal{M}}_{n-1}) \\ &\quad + \rho_{\mathcal{A}}(\mathcal{M}_n, \tilde{\mathcal{M}}_n)) \\ &\leq L_s^n \cdot \rho(\sigma(0), \sigma(0)) + \sum_{i=1}^n L_s^{n-i+1} \cdot \rho_{\mathcal{A}}(\mathcal{M}_i, \tilde{\mathcal{M}}_i) \\ &< \varepsilon \cdot \frac{L_s(L_s^n - 1)}{L_s - 1}. \end{aligned}$$

Thus, to ensure that $\sigma(0) \oplus \{\tilde{\mathcal{M}}_1, \dots, \tilde{\mathcal{M}}_n\}$ is a piece-wise strict β_r -approximation of σ , we only need to ensure that $\varepsilon \leq \frac{\beta_r(L_s - 1)}{L_s(L_s^n - 1)}$. As both n and L_s are fixed, we can choose ε to be as small as needed thus the desired fine resolution exists which concludes the proof. \square

Having established Lem. 2, we can finalize the first part of Thm. 2. Namely, we carefully set β_d and β_r , so that the final result is a piece-wise strict β -approximation.

Set $\beta_d = \beta_r = \sqrt{1 + \beta} - 1$. According to Lem. 1, there exists a finite sequence of motion primitives M_D in which every element has curvature $\kappa \in \{0, \kappa_{\max}\}$ such that the trajectory $\sigma_d = \sigma(0) \oplus M_D$ is a piece-wise strict β_d -approximation of σ .

Note that by construction σ_d is decomposable. Thus, according to Lem. 2, there exists a fine resolution $R(\sigma, \beta_r) = \{r_\ell, r_\theta\}$ and a finite sequence of motion primitives $M_{R(\sigma, \beta_r)}$ such that $\sigma_r = \sigma(0) \oplus M_{R(\sigma, \beta_r)}$ is a piece-wise

strict β_r -approximation of σ_d . Moreover, $M_{R(\sigma, \beta_r)} \subseteq \mathcal{M}_{\text{fs}}(R(\sigma, \beta_r), \{0, \kappa_{\text{max}}\})$ as the construction in the proof of Lem. 2 does not add new curvatures.

Finally, as $\beta_d = \beta_r = \sqrt{1 + \beta} - 1$, the trajectory σ_r is a piece-wise strict β -approximation of σ . This is because for every step above, we use segments of shorter lengths for the approximation, thus σ_r and σ satisfy $(\beta_d + \beta_r)$ point-pair-wise distance (condition (ii) and (iii)) in Def. 4. So we only need to take care of the first condition in Def. 4. Having $\beta_d = \beta_r = \sqrt{1 + \beta} - 1$ would provide us with $(1 + \beta_d)(1 + \beta_r) = 1 + \beta$, thus the trajectory length is also bounded, making every segments in σ_r local strict β -approximations of the corresponding segments in σ . By definition, σ_r is a piece-wise strict β -approximation of σ .

3) *Similar cost for piece-wise strict approximation:* We finish Thm. 2 by showing that the approximation of σ also achieves a desirable solution cost.

Lemma 3 (Similar cost for strict approximation). *If a collision-free trajectory σ' is a local strict β -approximation of another collision-free trajectory σ , and the cost function \mathcal{C} is well-behaved (characterized with $L_c, c_{\text{min}}, c_{\text{max}}$), then we have $\mathcal{C}(\sigma') \leq (1 + k \cdot \beta) \cdot \mathcal{C}(\sigma)$, where $k = \frac{L_c + c_{\text{max}}}{c_{\text{min}}}$.*

Proof. We have

$$\begin{aligned}
\mathcal{C}(\sigma') &= \int_0^l c(\sigma'(s)) ds \\
&= \int_0^l c(\sigma'(s)) ds + \int_l^{l'} c(\sigma'(s)) ds \\
&\leq \int_0^l \left(c(\sigma(s)) + L_c \cdot \beta \right) ds + \beta \cdot l \cdot c_{\text{max}} \\
&= \int_0^l \left(c(\sigma(s)) + L_c \cdot \beta + c_{\text{max}} \cdot \beta \right) ds \\
&= \int_0^l \left(1 + \frac{\beta(L_c + c_{\text{max}})}{c(\sigma(s))} \right) \cdot c(\sigma(s)) ds \\
&\leq \int_0^l \left(1 + \frac{\beta(L_c + c_{\text{max}})}{c_{\text{min}}} \right) \cdot c(\sigma(s)) ds \\
&= \left(1 + \frac{\beta(L_c + c_{\text{max}})}{c_{\text{min}}} \right) \cdot \int_0^l c(\sigma(s)) ds \\
&= \left(1 + \frac{\beta(L_c + c_{\text{max}})}{c_{\text{min}}} \right) \cdot \mathcal{C}(\sigma).
\end{aligned}$$

□

Apparently, if every piece of sub-trajectory is bounded, the sum of cost of all pieces is then also bounded. Thus, if a trajectory σ' is a piece-wise strict β -approximation of σ , then for a well-behaved cost, we also have $\mathcal{C}(\sigma') \leq (1 + k \cdot \beta) \cdot \mathcal{C}(\sigma)$.

C. Proof of Thm. 1

We are in a position to complete the proof of Thm. 1. Similarly to the proof for resolution completeness [3], we first develop the optimality proof for a simplified version of RCS*, termed RCS*_NP, which does not use node pruning as part of duplicate detection (line 7 in Alg. 1) and later

extend it to RCS*. For simplicity, we assume that both RCS* and RCS*_NP do not use the additional optimizations described in Sec. IV-B or Appendix A, which do not affect the validity of arguments used below.

1) *Resolution optimality of RCS*_NP:* Before we begin with the proof we mention that RCS*_NP terminates in finite time, which directly follows from our previous work [3, Thm. 1].

As a first step towards showing that Thm. 1 holds for RCS*_NP, we consider a reference trajectory σ^* and assume that conditions **C1**, **C2**, and **C3** are satisfied. According to **C1**, **C2**, and Thm 2, as σ^* is decomposable, for some $\beta > 0$, there exists a fine resolution $R(\sigma^*, \beta)$ with which a piece-wise strict β -approximation of σ^* can be constructed (Thm. 2). We denote such piece-wise strict β -approximation as σ_β^* . Moreover, it holds that $\mathcal{C}(\sigma_\beta^*) \leq (1 + k \cdot \beta) \cdot \mathcal{C}(\sigma^*)$. Recall (Thm. 1, **C2**) that $k = \frac{L_c + c_{\text{max}}}{c_{\text{min}}}$. Furthermore, we mention that the precise value of β will be assigned later on and for now we only assume that $\beta \in (0, \frac{\delta}{2}]$.

Next, we show that σ_β^* is valid and satisfies the desired goal tolerance, which implies that RCS*_NP will be able to find it. According to condition **C3**, σ^* is δ -robust. This implies that σ_β^* is at least $(\delta - \beta)$ -robust. Given that $\beta \leq \frac{\delta}{2}$, we further have σ_β^* is $\frac{\delta}{2}$ -robust. Thus for a cutoff resolution R_{min} that is fine enough, σ_β^* will be explored by the search tree constructed by RCS*_NP.¹

2) *Accounting for pruning:* Next, we describe how to account for pruning. Denote the sequence of motion primitives used to construct σ_β^* as $M_{\sigma_\beta^*} = \{\mathcal{M}_1, \dots, \mathcal{M}_n\}$. When $M_{\sigma_\beta^*}$ is sequentially applied to $\mathbf{x}_{\text{start}}$, we obtain a sequence of configurations $\{\mathbf{x}_0, \mathbf{x}_1, \dots, \mathbf{x}_n\}$, where $\mathbf{x}_0 = \mathbf{x}_{\text{start}}, \mathbf{x}_i = \mathbf{x}_{i-1} \oplus \mathcal{M}_i, i \in [1, n]$. For the rest of the proof, we use $M_{\sigma_\beta^*}[i, j] = \{\mathcal{M}_i, \dots, \mathcal{M}_j\}$ to denote a subsequence of $M_{\sigma_\beta^*}$. We also use $\mathbf{x} + M_{M_{\sigma_\beta^*}}[i, j]$ to denote the configuration after sequentially applying $\{\mathcal{M}_i, \dots, \mathcal{M}_j\}$ to \mathbf{x} .

If we run RCS*_NP, every configuration \mathbf{x}_i will be explored and σ_β^* will be constructed when the search terminates. However, if we run RCS*, we prune nodes using duplicate detection. Nevertheless, we now prove that, with similar node pruning, the search tree built with RCS* will explore a piece-wise strict $\frac{\delta}{2}$ -approximation of σ_β^* , which implies that RCS* returns a valid solution with sufficient goal tolerance. This will be done by showing that the same sequence of motion primitives $M_{\sigma_\beta^*}$ can be applied to configurations that are “similar” to $\mathbf{x}_0 \dots \mathbf{x}_n$ and the resultant plan $\tilde{\sigma}$ with low cost exists using the fact that $\tilde{\sigma}$ is “similar” to σ_β^* and that σ_β^* has $\frac{\delta}{2}$ -clearance. The rest of this proof formalizes this idea.

Recall that in **C4**, we require $d_{\text{sim}} < \frac{2}{\kappa_{\text{max}}} \sin \frac{\kappa_{\text{max}} \delta \ell_{\text{min}}}{2}$, which is the minimum positional difference between a node and its successor. This condition in **C4** guarantees that any successor node is not pruned by its parent node, which keeps

¹To be more precise, one needs to account for the cases where $R(\sigma^*, \beta)$ is not in the sequence of resolutions considered by the algorithm and we may introduce an additional error when approximating $R(\sigma^*, \beta)$ with R_{min} . However, this can be easily accounted for by using a finer resolution to approximate the target resolution $R(\sigma^*, \beta)$, similarly to Lem. 2.

the tree expanding. Now, let \mathbf{x}_i be the first configuration that is pruned because of a similar configuration (see Alg. 1, line 7). We will say that \mathbf{x}_i is *replaced* by the similar configuration \mathbf{x}'_i . We first consider the setting $i = 1$, and apply $M_{\sigma'}[2, n]$ to \mathbf{x}'_1 . According to condition **C4**, the maximal error accumulated to $\mathbf{x}'_n = \mathbf{x}'_1 + M_{\sigma'}[2, n]$ is $\xi_1 = \rho(\mathbf{x}'_n, \mathbf{x}_n) = L_s^{n-1} \cdot d_{\text{sim}}$. Similarly, when \mathbf{x}'_2 is replaced by \mathbf{x}''_2 , we apply $M_{\sigma'}[3, n]$ to \mathbf{x}''_2 and for $\mathbf{x}''_n = \mathbf{x}''_2 + M_{\sigma'}[3, n]$, the accumulated error is $\xi_2 = \rho(\mathbf{x}''_n, \mathbf{x}'_n) = L_s^{n-2} \cdot d_{\text{res}}$. The same analysis applies for $\{\mathbf{x}_3, \dots, \mathbf{x}_n\}$. In the worst case, \mathbf{x}_n can be replaced n times, which leads to the total accumulated error of

$$\begin{aligned} \xi &= \rho(\mathbf{x}_n^{(n)}, \mathbf{x}_n) \leq \rho(\mathbf{x}'_1, \mathbf{x}_1) + \dots + \rho(\mathbf{x}_n^{(n)}, \mathbf{x}_n^{(n-1)}) \\ &= \xi_1 + \dots + \xi_n = \frac{L_s^n - 1}{L_s - 1} \cdot d_{\text{sim}} \\ &< \frac{\delta}{2} \cdot \frac{L_s^n - 1}{L_s^H - 1} \leq \frac{\delta}{2}. \end{aligned}$$

Next we show that the solution $\tilde{\sigma}$ represented by the sequence of configurations $\mathbf{x}_0, \mathbf{x}'_1, \dots, \mathbf{x}_n^{(n)}$ satisfied goal tolerance (we show that $\tilde{\sigma}$ is valid after bounding its below). Indeed, due to the robustness of σ_β^* , we have that $\|\text{Prog}(\mathbf{x}_n) - g_{\text{goal}}\|_2 < \tau - \frac{\delta}{2}$. Thus,

$$\begin{aligned} &\|\text{Proj}(\mathbf{x}_n^{(n)}) - p_{\text{goal}}\|_2 \\ &\leq \|\text{Proj}(\mathbf{x}_n^{(n)}) - \text{Proj}(\mathbf{x}_n)\|_2 + \|\text{Proj}(\mathbf{x}_n) - p_{\text{goal}}\|_2 \\ &< \tau - \frac{\delta}{2} + \frac{\delta}{2} = \tau. \end{aligned}$$

This implies that even in the worst case where all possible replacements happen, the final configuration $\mathbf{x}_n^{(n)}$ still satisfies the required goal tolerance (see Fig. D).

3) *Incorporating solution cost and proving validity:* Next, we consider the cost of $\tilde{\sigma}$. Note that we only allow \mathbf{x}'_i to prune \mathbf{x}_i when $\mathcal{C}(\mathbf{x}'_i) \leq \mathcal{C}(\mathbf{x}_i^{(i-1)})$. Thus, for the final configuration along $\tilde{\sigma}$ we have

$$\begin{aligned} \mathcal{C}(\mathbf{x}_n^{(n)}) &\leq \mathcal{C}(\mathbf{x}_{n-1}^{(n-1)}) + \mathcal{C}(\mathbf{x}_{n-1}^{(n-1)}, \mathbf{x}_n^{(n)}) \\ &\leq \sum_{i=1}^n \mathcal{C}(\mathbf{x}_{i-1}^{(i-1)}, \mathbf{x}_i^{(i)}). \end{aligned}$$

It remains to bound the expression $\mathcal{C}(\mathbf{x}_{i-1}^{(i-1)}, \mathbf{x}_i^{(i)})$ for any $1 \leq i \leq n$. Denote by $\sigma_\beta^*(\mathbf{x}_{i-1}, \mathbf{x}_i)$ the trajectory segment from \mathbf{x}_{i-1} and \mathbf{x}_i along σ_β^* . Similarly define $\tilde{\sigma}(\mathbf{x}_{i-1}^{(i-1)}, \mathbf{x}_i^{(i)})$. We now show that $\tilde{\sigma}(\mathbf{x}_{i-1}^{(i-1)}, \mathbf{x}_i^{(i)})$ is local β_i -strict approximation of $\sigma_\beta^*(\mathbf{x}_{i-1}, \mathbf{x}_i)$ for $\beta_i = \frac{L_s^i - 1}{L_s - 1} \cdot d_{\text{sim}}$. To see that, first note that both trajectory segments use the same motion primitive and have the same length. Additionally, $\rho(\mathbf{x}_i^{(i)}, \mathbf{x}_i) \leq \frac{L_s^i - 1}{L_s - 1} \cdot d_{\text{sim}}$. Finally, An intermediate state \mathbf{x}' along the edge is also close to the corresponding state \mathbf{x} along the original edge, since they can be obtained by applying a motion primitive of a shorter length, and Lipschitz continuity of the system guarantees $\rho(\mathbf{x}', \mathbf{x}) \leq \frac{L_s^i - 1}{L_s - 1} \cdot d_{\text{sim}}$. Thus, since $\beta_i \leq \beta_n$, these local β_i -strict approximations are also local β_n -strict approximations.

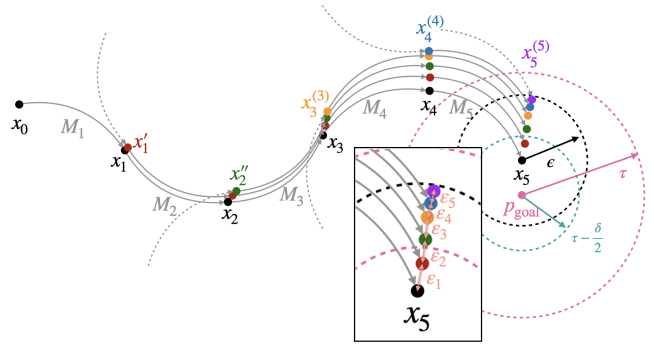


Fig. D: A 2D illustration of configuration pruning. σ_β^* is shown as black nodes, the plan after \mathbf{x}'_1 prunes \mathbf{x}_1 is shown as red nodes, the plan after \mathbf{x}''_2 prunes \mathbf{x}_2 is shown as green nodes, the plan after $\mathbf{x}_3^{(3)}$ prunes \mathbf{x}_3 is shown as yellow nodes, the plan after $\mathbf{x}_4^{(4)}$ prunes \mathbf{x}_4 is shown as blue nodes, and the pruning configuration $\mathbf{x}_5^{(5)}$ is shown as a purple node. The solid circular arrows represent elements in $M_{\sigma_\beta^*}$, and the dashed circular arrows represent connections to predecessors of the pruning configurations.

According to the similar-cost property of local strict approximation, we have that

$$\mathcal{C}(\mathbf{x}_{i-1}^{(i-1)}, \mathbf{x}_i^{(i)}) \leq (1 + k\beta_n) \cdot \mathcal{C}(\mathbf{x}_{i-1}, \mathbf{x}_i),$$

where k is as defined in **C2**. To summarize, the accumulated cost of $\tilde{\sigma}$ is as follows:

$$\begin{aligned} \mathcal{C}(\mathbf{x}_n^{(n)}) &\leq \sum_{i=1}^n \mathcal{C}(\mathbf{x}_{i-1}^{(i-1)}, \mathbf{x}_i^{(i)}) \\ &\leq (1 + k\beta_n) \cdot \sum_{i=1}^n \mathcal{C}(\mathbf{x}_{i-1}, \mathbf{x}_i) \\ &= (1 + k\beta_n) \cdot \mathcal{C}(\sigma_\beta^*) \\ &\leq \left(1 + k \cdot \frac{\delta}{2}\right) \cdot \mathcal{C}(\sigma_\beta^*) \\ &\leq \left(1 + k \cdot \frac{\delta}{2}\right) (1 + k\beta) \cdot \mathcal{C}(\sigma^*) \\ &= \left(1 + k \cdot \frac{\delta}{2} + k \cdot \beta + k^2 \cdot \frac{\delta \cdot \beta}{2}\right) \cdot \mathcal{C}(\sigma^*). \end{aligned}$$

It remains to determine the value of β to achieve a desired approximation factor of $1 + \epsilon$. So far we required $\beta \leq \frac{\delta}{2}$. To further guarantee that $\mathcal{C}(\mathbf{x}_n^{(n)}) \leq (1 + \epsilon) \cdot \mathcal{C}(\sigma^*)$ holds, we further require that $\beta \leq \frac{2\epsilon - k \cdot \delta}{k(2 + k \cdot \delta)}$. Thus we take $\beta = \min\left\{\frac{\delta}{2}, \frac{2\epsilon - k \cdot \delta}{k(2 + k \cdot \delta)}\right\}$. According to condition **C3** it follows that, $\delta \leq \frac{\epsilon}{k}$, so we always have $\beta > 0$.

It remains to show that $\tilde{\sigma}$ is valid. We have shown above that $\tilde{\sigma}(\mathbf{x}_{i-1}^{(i-1)}, \mathbf{x}_i^{(i)})$ is local β_n -strict approximation of $\sigma_\beta^*(\mathbf{x}_{i-1}, \mathbf{x}_i)$. This implies that for any configuration \mathbf{x}' along $\tilde{\sigma}(\mathbf{x}_{i-1}^{(i-1)}, \mathbf{x}_i^{(i)})$ there exists some corresponding configuration \mathbf{x} along $\sigma_\beta^*(\mathbf{x}_{i-1}, \mathbf{x}_i)$ such that $\rho(\mathbf{x}', \mathbf{x}) \leq \beta_n \leq \frac{\delta}{2}$. Due to the σ_β^* being $\frac{\delta}{2}$ -robust, we are guaranteed that the motion plan $\tilde{\sigma}$ is collision free.

To summarize, as long as the required conditions are satisfied, **RCS*** still finds a valid motion plan σ that satisfies $\mathcal{C}(\sigma) \leq (1 + \epsilon) \cdot \mathcal{C}(\sigma^*)$.